Supporting Information for "Using a Time-based Subarray Method to Extract and Invert Noise-derived Body Waves at Long Beach, California"

Jorge C. Castellanos[1], Robert W. Clayton[1], and Alan Juarez[2]

[1]Seismological Laboratory, Department of Earth and Planetary Sciences, Caltech, Pasadena, California, USA.

[2]Southern California Earthquake Center, University of Southern California, Los Angeles, California, USA.

Contents of this file

1. Figures S1 to S11

Additional Supporting Information (Files uploaded separately)

1. Caption for Dataset S1

2. Captions for Movies S1 to S4

Introduction

This section adds a number of additional details of the nature of the dataset and describes some of the final products of this investigation. The data used in this study is the property of Signal Hill Petroleum Inc., and permission from them is required to access it.

Dataset S1.

P-wave velocity model of Long Beach, California. The node spacing of the velocity model is 70 m and it can be downloaded from: http://dx.doi.org/10.22002/D1.1293. In

order to produce the cross-sections presented in Figures 11-12 of the main text, the velocity model was interpolated on a 10 m grid. The traveltime measurements used to produced the velocity model can also be downloaded from that site. The format of the file is as follows: (1) source longitude, (2) source latitude, (3) receiver longitude, (4) receiver latitude, (5) source easting (in km), (6) source northing (in km), (7) receiver easting (in km), (8) receiver northing (in km), (9) source elevation (in m), (10) receiver elevation (in m), (11) L2 Misfit of the double-beamforming (in s^2), (12) theoretical arrival time (in s), (13) picked arrival time (in s), (14) signal-to-noise ratio, (15) normalized correlation coefficient of the pick with its respective waveform template. The coordinates of the sources and receivers are those of the geographic centers of the subarrrays.

Movie S1.

Example of construction of receiver subarrays (orange circles) for a given source subarray (green circles)

Movie S2.

Reconstructed wavefield propagating away from a virtual source after applying double beamforming.

Movie S3.

Horizontal slices of the P-wave velocity model as a function of depth. To emphasize the lateral velocity variations, each slice is normalized to its maximum value. As in the main text, blue is fast and green is slow.

Movie S4.

Carson Mb2.5 earthquake wavefront propagating through the Long Beach array. The time from the origin of the earthquake is shown in the upper left panel.

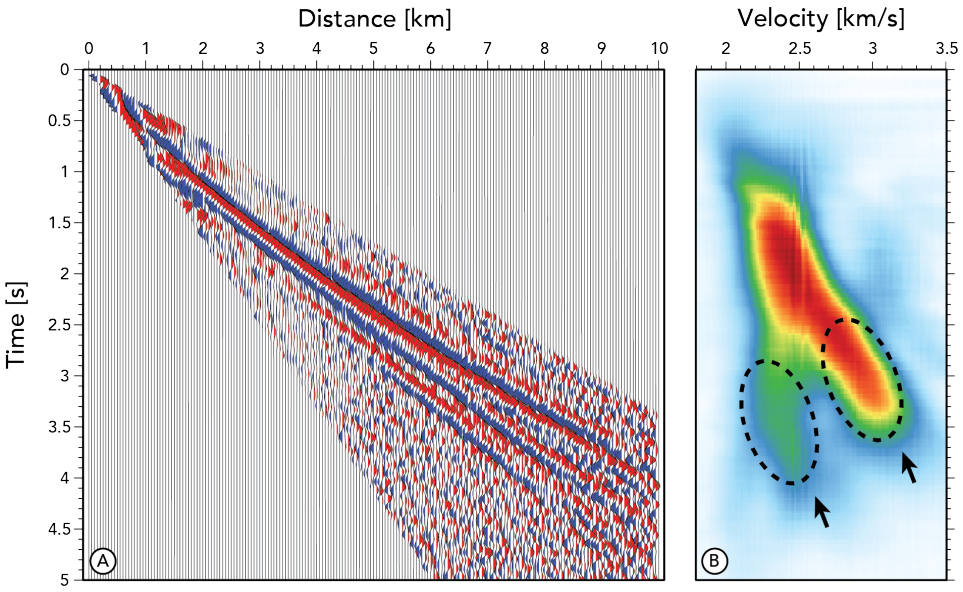

Figure S1. (A) First 5 seconds of the stacked cross-correlations windowed around the expected P-wave time of arrival. (B) Slant-stack image of the record section in (A). The dashed ovals mark the two prominent energy strands in the velocity space that correspond to the multiple P-wave arrivals that are present in the stacked record section.

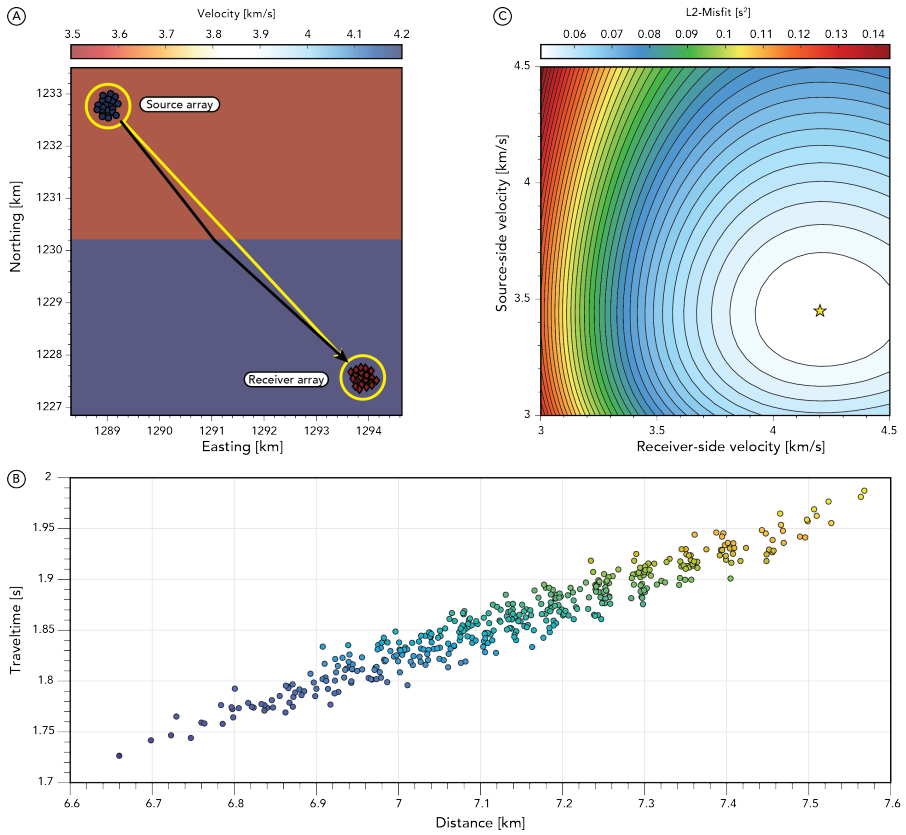

Figure S2. Synthetic exercise performed to test the strength of bias that may arise from assuming a direct propagation path in the double-beamforming. (A) Geographic map showing the source and receiver arrays plotted on top of the assumed velocity model (the source side velocity is 3.5 km/s and the receiver side velocity is 4.2 km/s). The yellow arrow marks the direct path of the ray while the black arrow marks the true propagation path of the ray. (B) Synthetic traveltimes from each source to each station computed from the assumed velocity model. (C) Entire source and receiver side velocity space of the double-beamforming after fixing the optimum beam azimuth to the azimuth between the geographic center of the source and receiver arrays. The best-fitting pair of velocities is marked by the yellow star (retrieved source side velocity is 3.45 km/s and retrieved receiver side velocity is 4.2 km/s). Note that, under the straight-ray assumption, the presence of an exceedingly large velocity contrast between the source and receiver sides (∼20%) causes an underestimation of the source side velocity of only 0.05 km/s. This inaccuracy in the double-beamforming becomes even smaller as the velocity contrast between the source side and receiver side decreases.

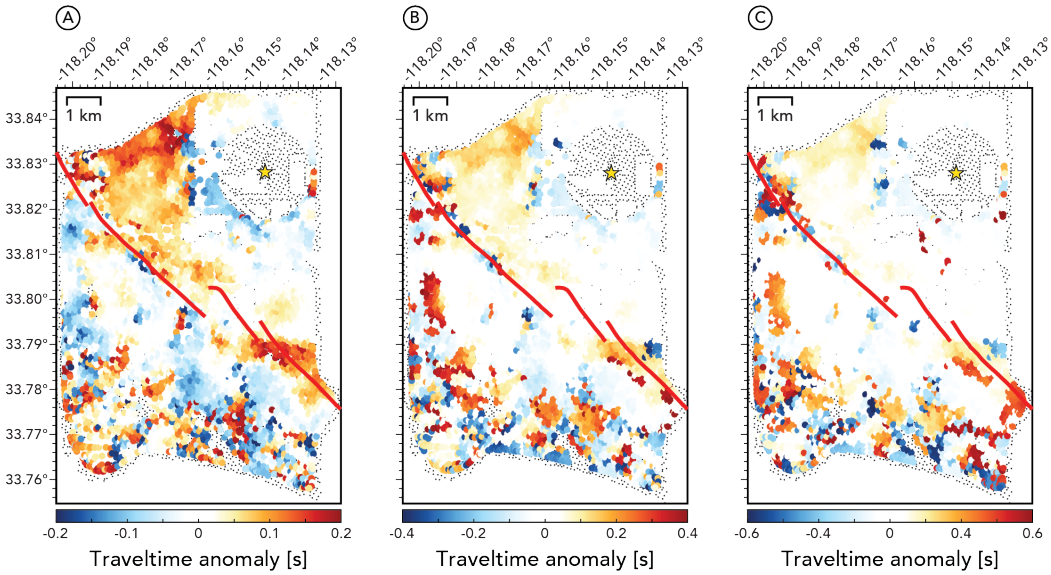

Figure S3. Traveltime anomaly distributions using a ±0.2 s (A), a ±0.4 s (B), and ±0.6 s (C) tolerance time windows in the double-beamforming. Note that the the first-order features of the maps are the same regardless of the length of the tolerance window, and how most of the velocity variations are well-captured with the ±0.2 s window length.

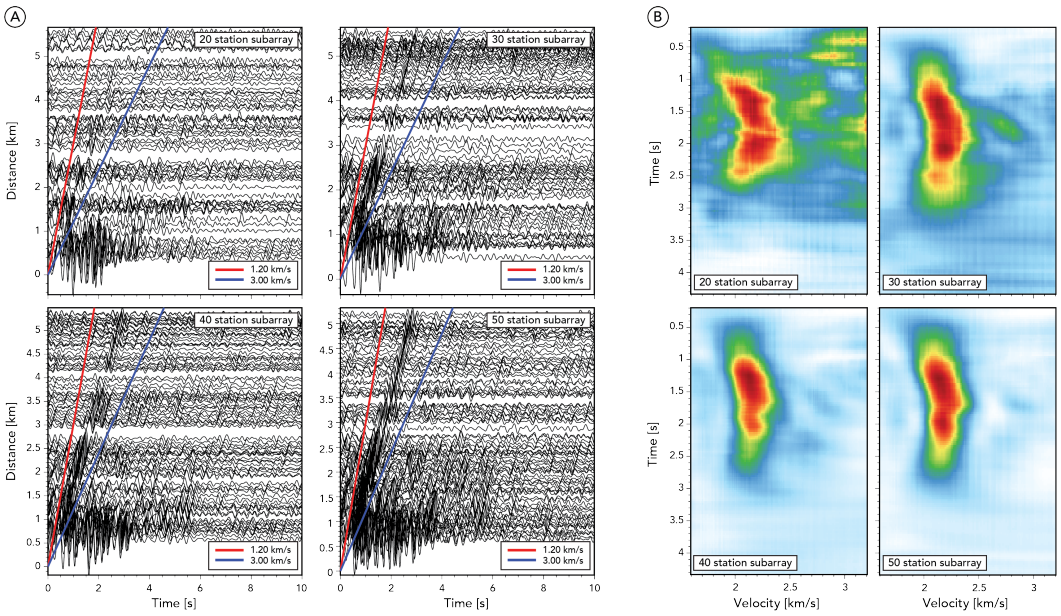

Figure S4. Double-Beamforming results using different sized source and receiver subarrays. (A) Record sections of beams constructed from 20, 30, 40 and 50 station subarrays. The red and blue lines mark the expected time-of-arrival of the refracted P-wave. (B) Slant-stack image of the record sections in (A). A clear increase in the signal-to-noise ratio of the traces is observed as the number of station increases. For this study, we chose to use 30 station-sized arrays to perform the double-beamforming as it qualitatively provides an adequate tradeoff between signal-to-noise ratio and resolution.

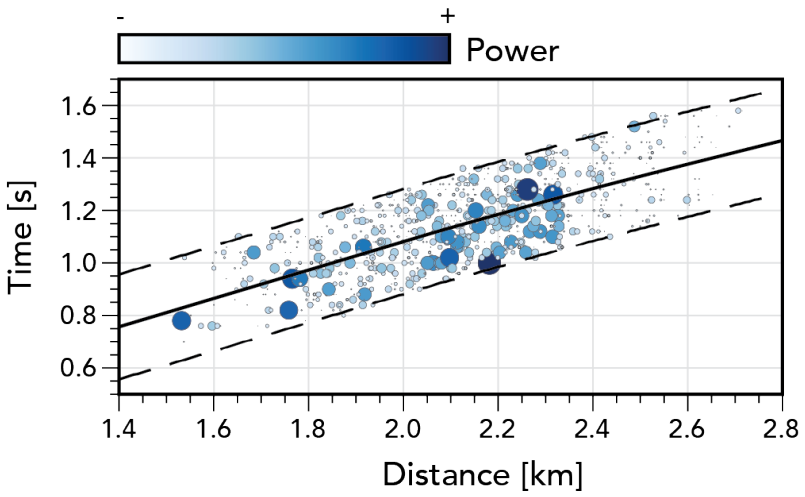

Figure S5. Timing of all the spectra peaks found in the 900 cross-correlations that are within their respective P-wave time windows. These traveltime picks correspond to those used to build the beam presented in Figure 6 of the main text. Both the size and color of the markers are proportional to their absolute spectral power. The black line marks the predicted time of arrival and the dashed lines represent the length of the tolerance time window.

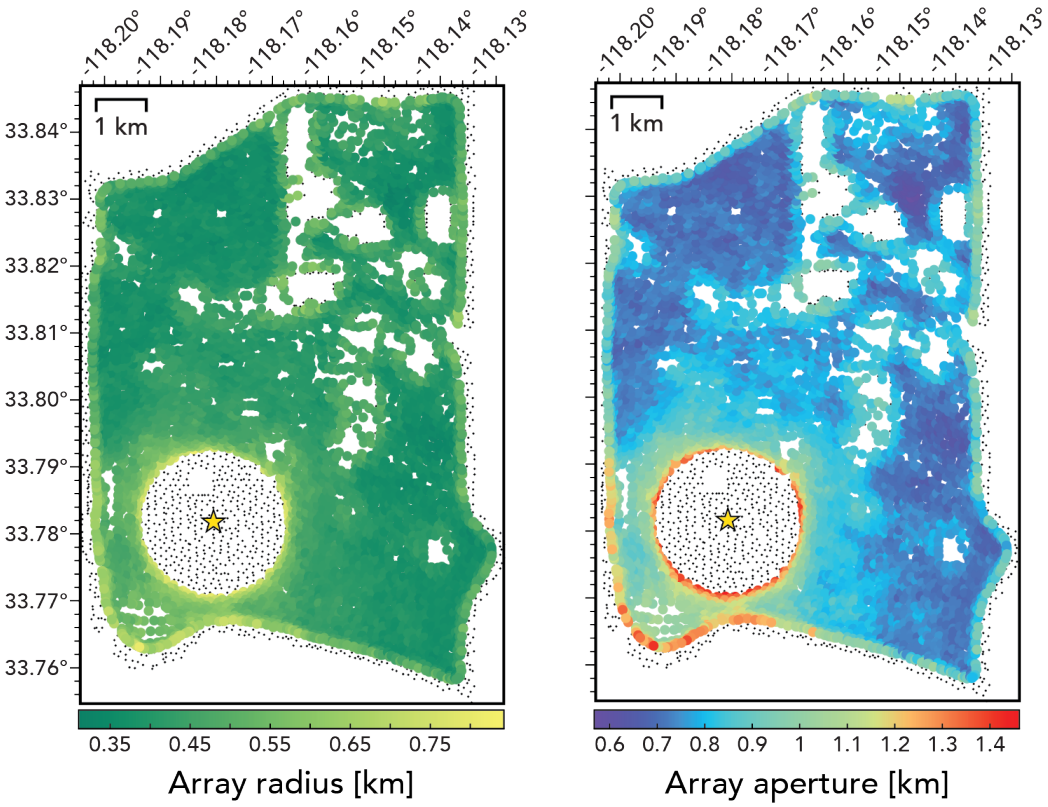

Figure S6. Double-Beamforming results using different sized source and receiver subarrays. (A) Record sections of beams constructed from 20, 30, 40 and 50 station subarrays. The red and blue lines mark the expected time-of-arrival of the refracted P-wave. (B) Slant-stack image of the record sections in (A). A clear increase in the signal-to-noise ratio of the traces is observed as the number of station increases. For this study, we chose to use 30 station-sized arrays to perform the double-beamforming as it qualitatively provides an adequate tradeoff between signal-to-noise ratio and resolution.

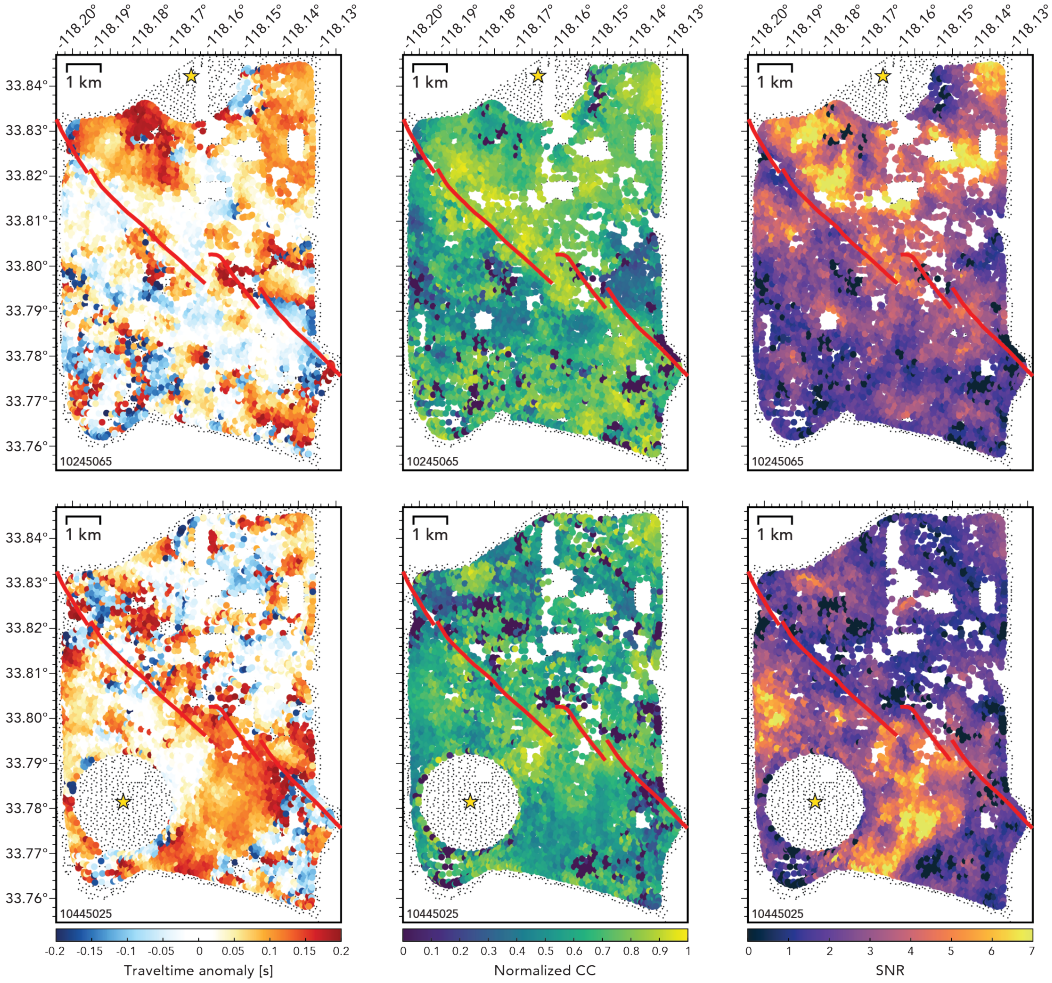

Figure S7. Traveltime measurements for two virtual sources. The left panels show the distribution of the traveltime differences between the picked time and the theoretical arrival. The middle panels show the normalized correlation coefficient between each picked phase with their respective waveform template. The right panels show the signal- to-noise ratio of the beams. Note how the CC and SNR are generally higher for beams constructed on similar sides of the fault.

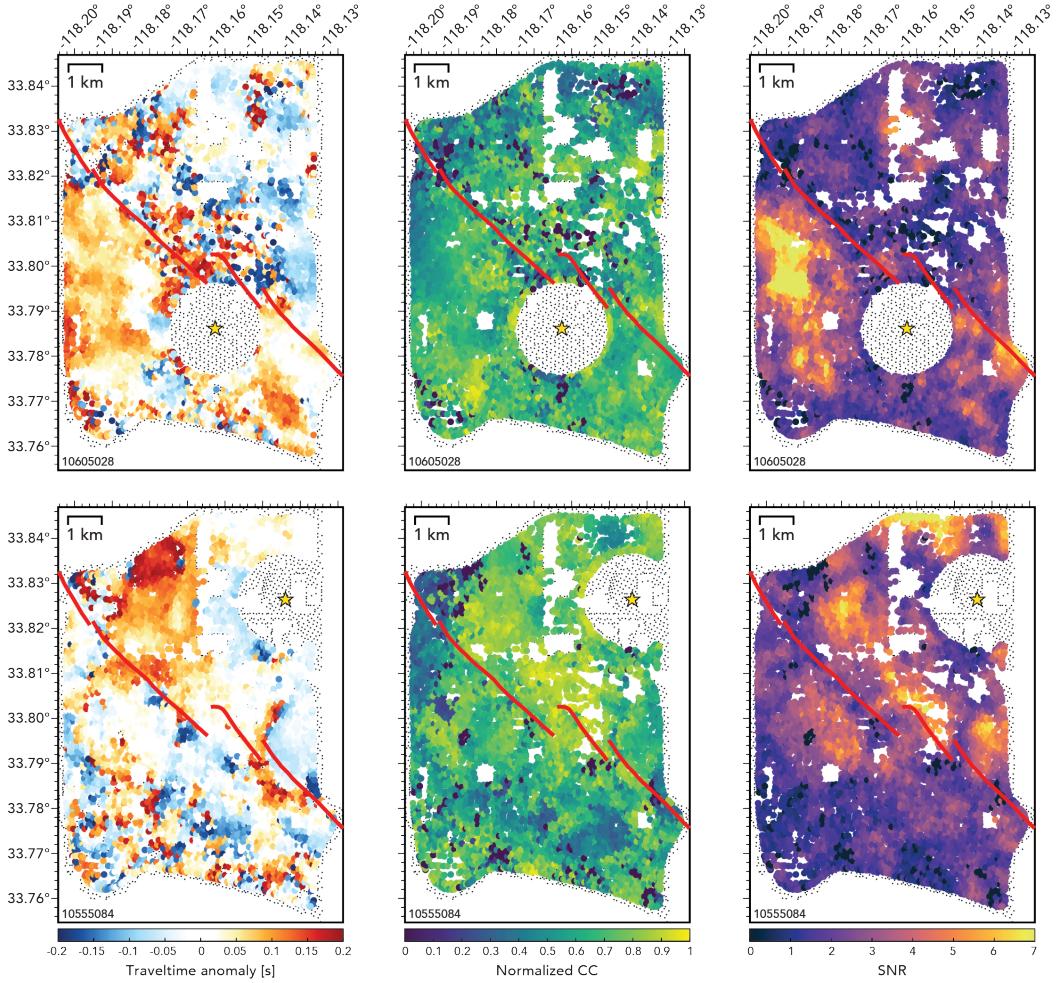

Figure S7. Traveltime measurements for two virtual sources. The left panels show the distribution of the traveltime differences between the picked time and the theoretical arrival. The middle panels show the normalized correlation coefficient between each picked phase with their respective waveform template. The right panels show the signal- to-noise ratio of the beams. Note how the CC and SNR are generally higher for beams constructed on similar sides of the fault.

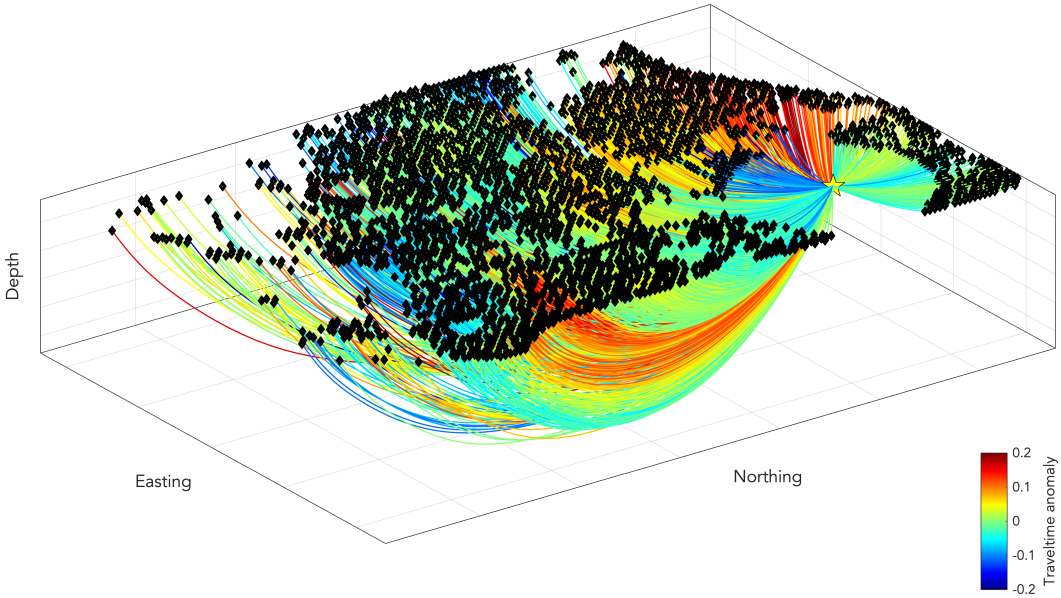

Figure S8. Example of 3D raytracing for a single shot gather using the inverted 1D velocity model in Figure 2B. The yellow star marks the location of the virtual source and the black diamonds mark the location of the receivers. Each ray is color-coded by its traveltime anomaly (in seconds). To generate this image, we only used traveltime measurements that had a correlation coefficient larger than 0.5 with their respective waveform templates and a signal-to-noise ratio larger than 2.

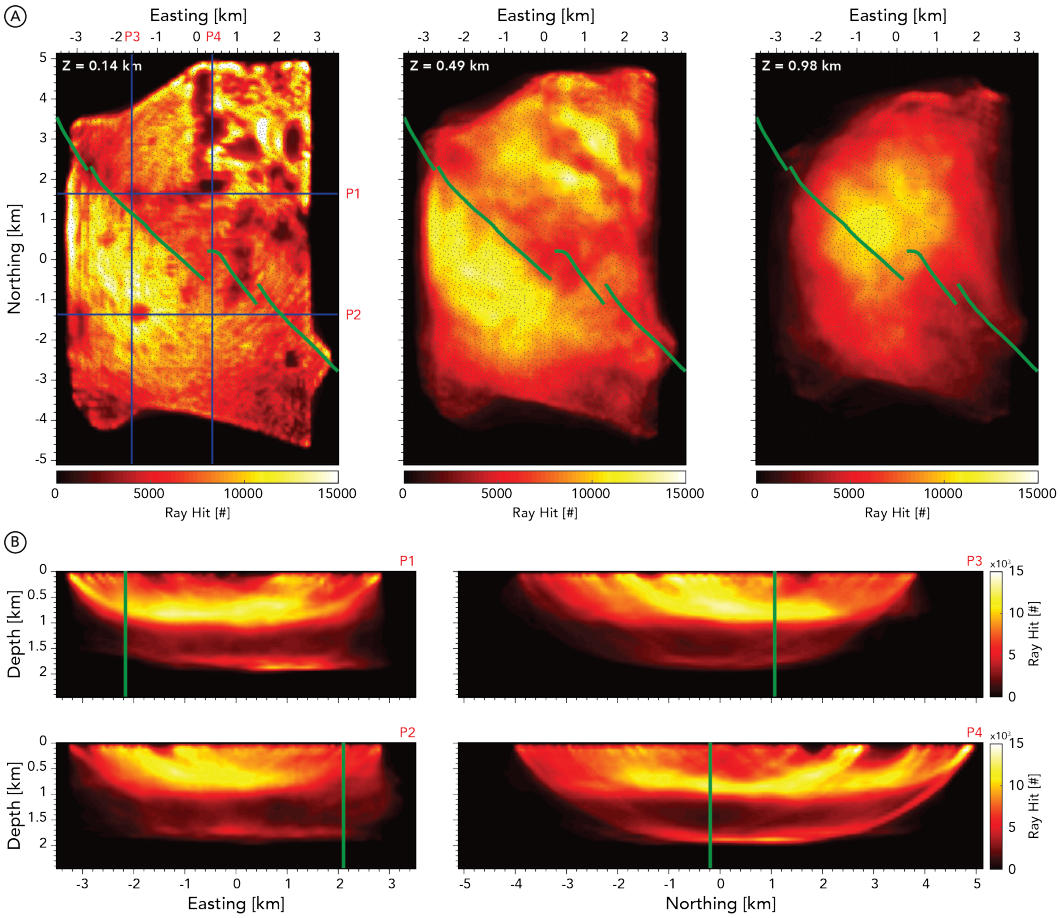

Figure S9. Horizontal (A) and vertical (B) slices of the number of rays at each cell for the traveltime tomography. The depth of the horizontal slices is given at the upper right corner of each panel (0.14 km, 0.49 km and 0.98 km). The blue lines in the leftmost panel in A show the location of the vertical slices in B (P1, P2, P3 and P4). For this set of plots, the local coordinates have been shifted to the center of the survey. The green lines in every panel mark the major strands of the Newport Inglewood fault.

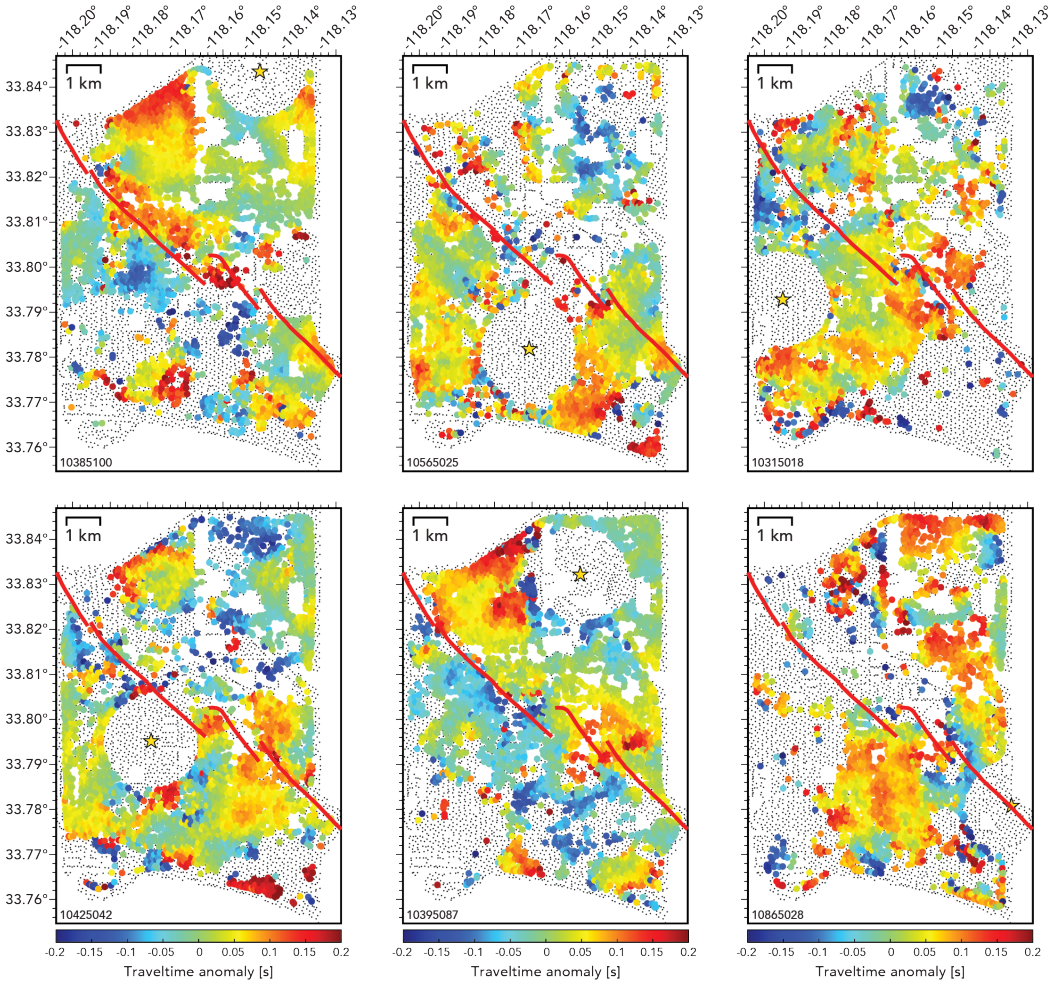

Figure S10. Traveltime anomaly maps for 6 different virtual sources after filtering by CC and SNR. For each panel, the black circles in the background mark the location of the stations and the yellow star marks the location of the virtual source. To generate these images, we only used traveltime measurements that had a correlation coefficient larger than 0.5 with their respective waveform templates and a signal-to-noise ratio larger than 2.

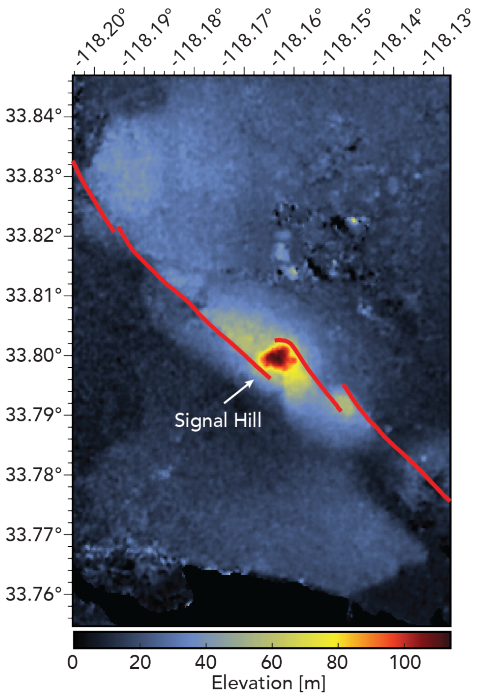

Figure S11. Elevation map of Long Beach, California. The major strands of the Newport Inglewood fault are denoted by red lines.